Tm³⁺/Yb³⁺co-doped SrF₂ up-conversion phosphors for non-invasive optical thermometry: ratiometric approach using thermal and non-thermal coupled fluorescent emission bands

Nikifor Rakov[1] · Simone A. Vieira[1] · Anderson S. L. Gomes[1,2]

Abstract

To explore novel up-conversion (UC) system for optical temperature sensing, a series of Tm/Yb:SrF₂ fluoride powders were fabricated employing a combustion synthesis (CS) technique. When Tm/Yb: SrF₂ samples were excited by near-infrared radiation (~ 980 nm), four UC emission bands at ~ 477 nm ($^1G_4 \rightarrow {}^3H_6$), ~ 649 nm ($^1G_4 \rightarrow {}^3F_4$), ~ 700 nm ($^3F_{2,3} \rightarrow {}^3H_6$) and ~ 771 nm ($^3H_4 \rightarrow {}^3H_6$) were observed. Non-contact thermal sensing performances based on temperature-dependent fluorescence intensity ratio (FIR) technique of thermally and non-thermally coupled energy levels were estimated in the range from 298 to 573 K. The co-doped phosphor showed, at 298 K, a maximum relative sensitivity S_{NTr} of ~ 2.2%K⁻¹ for the non-thermally coupled energy levels [($^3H_4 \rightarrow {}^3H_6$)/ ($^1G_4 \rightarrow {}^3H_6$)] and a maximum relative sensitivity S_r of ~ 1.7%K⁻¹ for the thermally coupled levels [($^3F_{2,3} \rightarrow {}^3H_6$)/($^3H_4 \rightarrow {}^3H_6$)]. These outcomes show a good temperature-sensing performance when the non-thermally coupled levels with different temperature dependences were selected as the thermometric parameters. Hence, the Tm/Yb: SrF₂ UC system has a promising prospect as optical temperature-sensing material.

Keywords Optical thermometry · Fluorescence intensity ratio · Energy transfer · Combustion synthesis

1 Introduction

Trivalent rare earths (RE) ions are recognized as outstanding active materials for application in luminescence-based devices. The frequently detected luminescence phenomenon of RE ions embedded in inorganic hosts has its cause regularly in photon up-conversion (UC) processes [1–6]. UC emission is a nonlinear procedure generated after the successive absorption of low-energy photons followed by the emission of high-energy photons [1–6]. At present, UC luminescent materials have been widely used in temperature sensing, a three-dimensional solid-state display, solar cells, bioluminescence labeling, solid-state lasers, and so on and have become an important part of these key technologies which have attracted more and more attention of scientists

[1–6]. Among all trivalent rare earth ions, thulium (Tm³⁺) is an important luminescence center, which exhibits intense visible and infrared luminescence, mainly concentrated in visible light, emitting in the blue: $^1G_4 \rightarrow {}^3H_6$ of Tm³⁺ and in the red: $^1G_4 \rightarrow {}^3F_4$ transitions of Tm³⁺, or in the infrared, arising from the $^3F_{2,3} \rightarrow {}^3H_6$ and $^3H_4 \rightarrow {}^3H_6$ states of Tm³⁺ [7–10]. However, UC materials doped with Tm³⁺ ions have inefficient absorption at the near-infrared and consequently cannot be efficiently pumped at the wavelength of 980 nm. Hence, in order to improve the pumping efficiency, a clever alternative is to co-dope the host material with a near-infrared sensitizer such as ytterbium (Yb³⁺) [7–10]. As a suitable sensitizer, Yb³⁺ ion offers a broad and high absorption band around ~ 1 μm and its single electronic transition $^2F_{5/2} - {}^2F_{7/2}$ matches among intermediate states of Tm³⁺, which benefits energy transfer processes between Yb³⁺ and Tm³⁺. As a result, current studies on Tm³⁺/Yb³⁺ co-doped materials have been reported in different host structures [7–10].

Concerning photonics applications, temperature sensing is one of the potential applications of UC materials [11–13]. Commonly, RE-based thermal sensors exploit the intensity ratio approach, which oversees temperature-induced variations in the fluorescence intensity ratio (FIR)

✉ Nikifor Rakov
nikifor.gomez@univasf.edu.br

1 PPG - Ciência dos Materiais, Universidade Federal do Vale do São Francisco, Juazeiro, BA 48902-300, Brazil

2 Departamento de Física, Universidade Federal de Pernambuco, Recife, PE 50670-901, Brazil
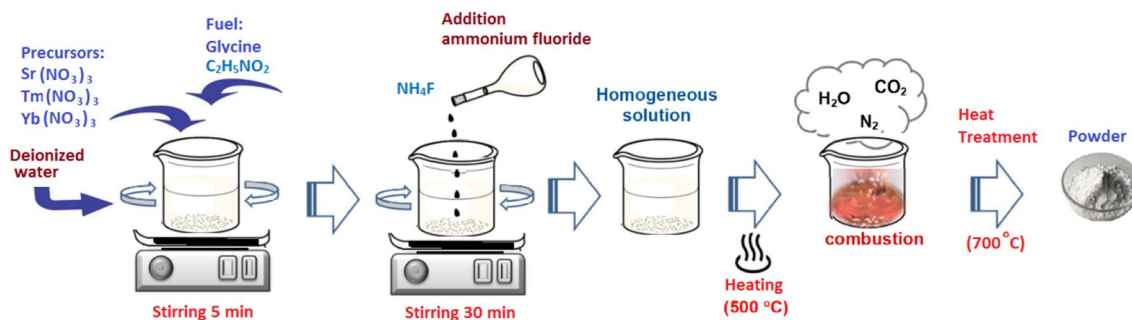
Scheme 1. Diagram of the main steps of the combustion synthesis used to produce strontium fluoride powders

between two emission bands [13]. In particular, optical thermometry based on the FIR method from two thermally coupled energy levels (TCL) of RE ions has gained more attention. For example, among RE ions, TCL may be establish in ($^2H_{11/2}$ / $^4S_{3/2}$) levels of Er^{3+} [14], ($^3F_{2,3}$ / $^3H_4$) levels of Tm^{3+} [15], splitting levels of two different sub-levels of Nd^{3+} ($^4F_{3/2}$: R1 and R2) [16, 17], and so on. Basically, the ratiometric readout of the fluorescence intensity changes of two TCL is based on thermal equilibrium and ensured by the Boltzmann distribution law [13]. Moreover, the FIR Boltzmann-dependent ratiometric thermometer is concomitant with TCL whose energy separation ΔE, usually restricted to 200–2000 cm^{-1}, is proportional to its thermometric sensitivity according to the Boltzmann-type population statistics. In this way, an additional ratiometric-based luminescent thermometer technique is essential in order to overcome the limitations of the energy separation ΔE based on the emission intensity of TCL and which could functionate as a perfect counterpart of the FIR Boltzmann-dependent ratiometric thermometer. Accordingly, the FIR technique based on non-thermally coupled levels (NTCL) appears to be an effective complement to a better sensitivity of the FIR technique associated with thermally coupled levels. Essentially, the ratiometric readout of the NTCL is based on the temperature sensing founded on the thermalization processes of one emission state with respect to the other metastable state which are non-thermally coupled levels [18, 19]. Being that, this challenging method based on NTCL seems to be an effective strategy to measure the thermally induced changes of the luminescence intensity for monitoring the optical temperature-sensing properties.

On the other hand, magnificent UC temperature sensors either need appropriate host materials. Thus, the selection of the appropriate host material is important to increase the UC luminescent efficiency of RE ion-based materials [16, 17, 20]. Commonly, fluoride compounds such as CaF_2 and SrF_2 are very popular as host materials for RE ions, owing mainly to their low phonon energies (~ 370 cm^{-1})

that favors RE ion luminescence and a high luminescent quenching concentration [16, 21–24].

Following the described influential guiding, we have systematically examined the UC properties of Tm^{3+}/Yb^{3+} co-doped SrF_2 ceramic powders synthesized using combustion methodologies (CS) [25], followed by a detailed investigation of their UC luminescence under 980 nm light excitation and present its performance in optical temperature sensing based on the fluorescence intensity ratio (FIR) method (i) considering a Boltzmann distribution of electronic population in the thermally coupled states ($^3F_2$, $^3F_3$), and $^3H_4$ of Tm^{3+} [15, 26] and (ii) taking into account the fluorescence intensity variations for the non-thermally coupled level states ($^3H_4$) and ($^1G_4$) of Tm^{3+} ions. The current phosphor was also compared with other typical UC systems to show their advantages in optical temperature sensing. The results indicate that Tm^{3+}/Yb^{3+} co-doped SrF_2 emitting phosphor is a good candidate for luminescent thermometry application.

2 Samples preparation

Tm^{3+} and Yb^{3+} co-doped SrF_2 powders were prepared by a simple CS route [11]. The main steps of the method of preparation used to fabricate strontium fluoride powders are shown in Scheme 1. Strontium nitrate reagem grade $Sr(NO_3)_3$ (Aldrich, 99.9%), thulium nitrate hexahydrate $Tm(NO_3)_3 \cdot 6 \cdot H_2O$ (Aldrich, 99.9%), ytterbium nitrate pentahydrate $Yb(NO_3)_3 \cdot 5H_2O$ (Sigma, 99.99%), ammonium fluoride NH_4F (Sigma, p.a.) and glycine $C_2H_5NO_2$ (Sigma, 99.95%) as a fuel were used as purchased. Deionized water was applied in the entire procedure.

Briefly, stoichiometric amounts of metal nitrates were first dissolved in a minimum amount of deionized water (15 ml). Subsequently, the appropriate amount of glycine was added to the above blend under constant stirring. The mixed solution was continually stirred for about 5 min. At that time, an aqueous solution of ammonium fluoride was added dropwise to the previous mixture, still under constant stirring, with a slight excess of fluoride ions with respect to

the stoichiometric required. Next, the mixed solution was kept under constant mechanical stirring for 0.5 h and at room temperature until it was transformed into a milky solution. Finally, the resultant liquid combination was placed in a pre-heater furnace (500 ºC) for 20 min until excess free water evaporated and spontaneous ignition occurred resulting in a fine white powder. Once cooled and grounded, the obtained powder product was sintered at 700 ºC for 4 h in ambient atmosphere. Finally, the corresponding $[Sr_{(1-x-y)}Tm_xYb_y]F_2$ samples with different concentrations: SrF_2: (8 wt%) Yb^{3+} / x%Tm^{3+} (x is the wt% concentration of Tm^{3+}, i.e., 0.05%, 0.2% and 0.5%) and SrF_2: (0.2 wt%) Tm^{3+}/ y%Yb^{3+} (y is the wt% concentration of Yb^{3+}, i.e., 6%, 8%, and 10%) were obtained.

2.1 Samples characterization

To analyze the crystalline structure of the samples, X-ray powder diffraction (XRPD) analysis was performed by use of a Bruker AXS D8 Advance (CuK$_\alpha$ radiation, 40 kV and 40 mA) operating in a Bragg–Brentano θ/θ configuration. XRPD pattern was collected in a flat geometry with steps of 0.02 degrees and accumulation time of 30 s per step.

UC luminescence of the phosphor was obtained using the focused beam (f = 6 cm) of a commercial near-infrared CW laser diode (λ = 980 nm, 210 mW, BW-TEK). The UC luminescence, acquired in a reflection mode, was collected through an optical fiber attached to a compact spectrometer (Ocean Optics-USB4000), with an optical resolution of ~ 0.3 (FWHM). For temperature analysis, the fresh powder was compacted and held inside a small metallic holder (5 mm diameter, 2 mm height) and placed over a temperature-controlled hot plate. The scattered/reflected laser light at the output face of the sample was rejected by use of a cut-off optical filter.

3 Results and discussion

3.1 Structural analysis

The crystal structure of heat-treated SrF_2: (8 wt%) Yb^{3+} / x%Tm^{3+} (x is the wt% concentration of Tm^{3+}, i.e., 0.05%, 0.2% and 0.5%) and SrF_2: (0.2 wt%) Tm^{3+}/ y%Yb^{3+} (y is the wt% concentration of Yb^{3+}, i.e., 6%, 8%, and 10%) co-doped powders was identified by XRD measurement. As depicted in Fig. 1, the diffraction peak potions of all the calcined samples are identified with pure face-centered cubic phase (space group: Fm3m) with standard data for SrF_2 (JCPDS no.06–0262), and no other impurity peak is detected, suggesting the formation of phase pure material. In the current work, the heat treatment temperature selected was 700 °C.
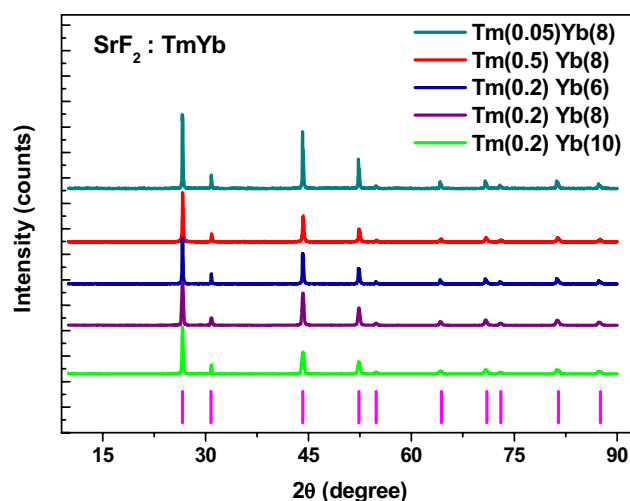

Fig. 1 XRPD pattern of Tm^{3+}/ Yb^{3+}: SrF2 powder samples heat treated at 700 °C for 4 h

3.2 UC Luminescence analysis:

The room temperature UC emission spectra of SrF_2: Tm^{3+}/ Yb^{3+}fluoride powders under continuous infrared light excitation (λλ = 980 nm) are collected and presented in Fig. 2. Figure 2(a) shows the UC emission in the range of 440–860 nm for (0.2 wt%) Tm^{3+}/xYb^{3+}(x = 6.0, 8.0 and 10 wt%) co-doped SrF_2 fluoride powders. The UC emission spectra consist of two emission bands in the visible region with UC bands peaked at ~ 477 nm and ~ 649 nm, which are associated with the $^1G_4 \rightarrow {}^3H_6$ (~ 21*10³ cm⁻¹) and the $^1G_4 \rightarrow {}^3F_4$ (~ 15*10³ cm⁻¹) transitions of Tm^{3+} ions, respectively, and two emission bands in the NIR region, centered at ~ 700 and ~ 771 nm, corresponding to the $^3F_3 \rightarrow {}^3H_6$ (~ 14*10³ cm⁻¹) and $^3H_4 \rightarrow {}^3H_6$ (~ 13*10³ cm⁻¹) transitions of Tm^{3+}, in that order [27]. No emission peak positions shifted were observed, whereas doping content of Yb^{3+} ions was varied. Likewise, it is observed that the emission intensity of Tm^{3+} ions increased at first with the growth of Yb^{3+} concentration, attained the maximum value at the doped concentration of 8.0 wt% and subsequently decreased once Yb^{3+}ion concentration exceeded 8.0 wt% due to concentration quenching effect [26, 28]. Referring on the energy level positions (cm⁻¹) of the emission bands of Tm^{3+}, in the literature, Carnall et al. [27] have investigated the spectroscopic properties of Tm^{3+} doped LaF_3 single crystal. Therefore, based on the above outcomes [27], the emissions peaks observed in Fig. 2a are originating from the intra-configurational transitions of the Tm^{3+} ions and assigned them the corresponding emission transition in cm⁻¹ units.

For the optimization of dopant ions concentration of Tm^{3+} ion, a series of co-doped Tm^{3+}:Yb^{3+}: SrF_2 phosphors have been prepared as a function of the Tm^{3+}concentration
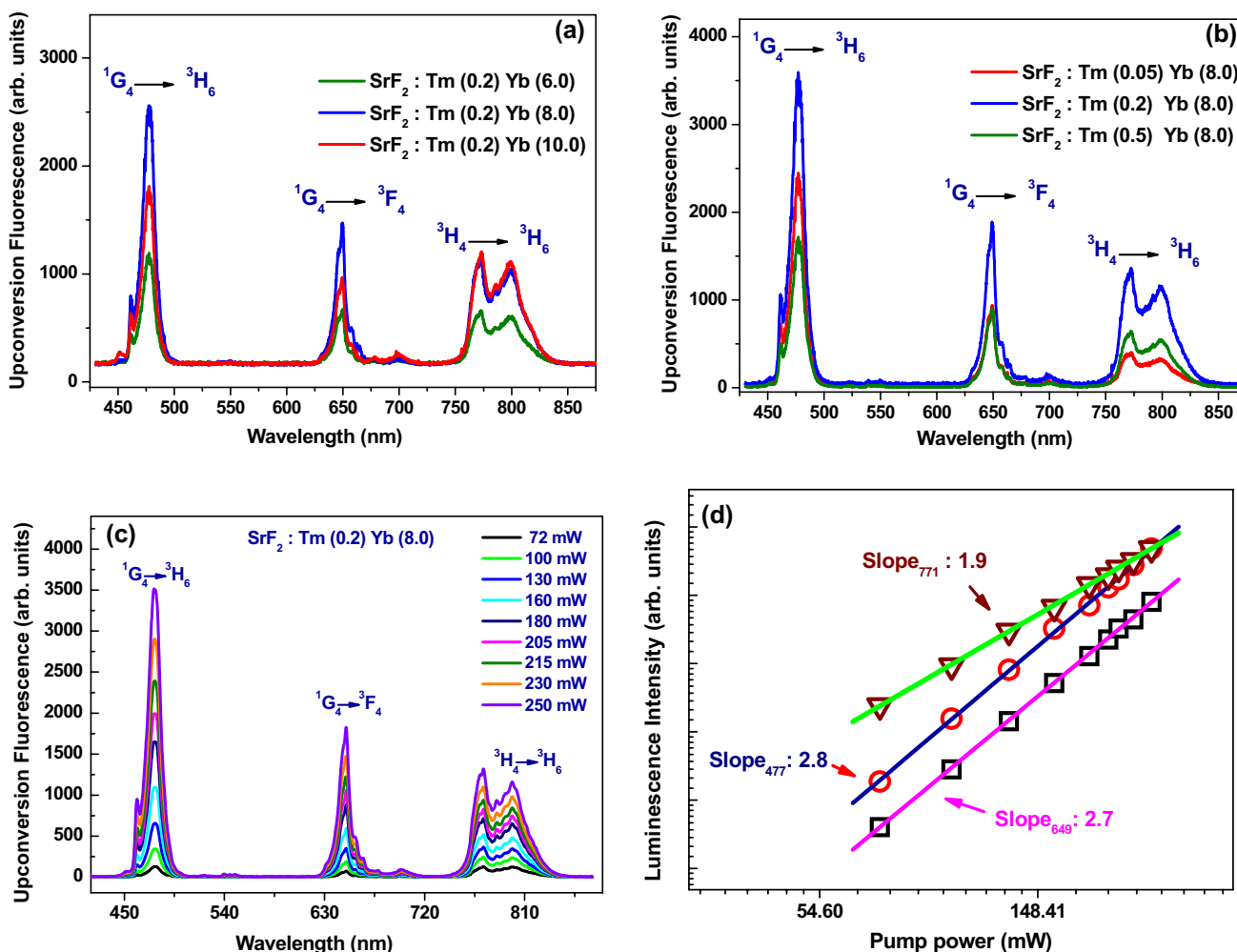
Fig. 2 **a** The UC emission spectra of SrF$_2$: (0.2 wt%) Tm^{3+}: x%Yb^{3+}, (x = 6.0; 8.0 and 10.0) co-doped fluoride powders for excitation at λ = 980 nm at room temperature. **b** UC luminescence spectra of SrF$_2$: y%Tm^{3+}:(8wt%) Yb^{3+}, (y = 0.05; 0.2 and 0.5) co-doped powder samples under near-infrared excitation at room temperature. **c** The UC luminescence intensity of Tm^{3+}: Yb^{3+} (0.2:8.0 wt%) co-doped SrF$_2$ powder under different pump power densities. **d** Log–log plot of the UC signal intensity as a function of the excitation power for Tb^{3+} co-doped with Yb^{3+}: SrF$_2$ powders. The fitted lines and the obtained slopes are also provided

(0.05, 0.2 and 0.5 wt%) and at fixed Yb^{3+} ions doped concentration (8.0 wt%). Figure 2b depicts the UC spectra in the visible-NIR region as a function of the Tm^{3+} concentration. The optimum concentration was achieved for Tm^{3+}:Yb^{3+}: SrF$_2$ co-doped sample corresponding to Tm^{3+} (0.2wt%):Yb^{3+}(8.0wt%), and above this critical concentration, a reduction in the emission intensity is noted. The decrease in the overall luminescence intensity with the increase of the Tm^{3+} percentage is an indication of the concentration quenching influence. This effect could be elucidated by the presence of the energy transfer mechanism between the nearest dopant ions (activator → activator *or* sensitizer ↔ activator). As the concentration of Tm^{3+} increases, the average distance between the RE ions decreases, contributing significantly to a strong interaction between adjacent Tm^{3+} and, as a result, improving the

non-radiative relaxation responsible for the reduction of the UC luminescence [26, 28]. All the samples were evaluated in the same settings.

To gain further understanding into the UC luminescence mechanisms, a relationship between UC intensity and excitation power was employed. After identifying the optimum sample concentration, Fig. 2c presents the UC emission spectra for co-doped SrF$_2$:Tm^{3+}(0.2wt%): Yb^{3+}(8.0wt%) sample submitted to various excitation densities from laser operating at 980 nm. It can be observed that the emission intensity of Tm^{3+} exhibits a continuous growth as the excitation density increases. The number of NIR photons responsible for these UC emissions can be calculated. Considering that the UC process is not saturated, the integrated UC luminescence intensity signal should obey the relationship $I_{UP} \propto P_L^n$, $I_{UC} \propto P_L^N$ $I_{UC} \propto P_L^N$ where *n* is the number of NIR

pump photons required to populate the upper emitting state, and P_L is the intensity of excitation source. Figure 2d shows a logarithmic plot of the pump power dependence of the UC intensities at 477 nm (blue), 650 nm (red) and 771 nm (NIR) for one of the samples shown in Fig. 2b. From the pump power dependence analysis, the number n of the infrared photons necessary to generate each UC photon is calculated through the slope of the linear best-fit. Note that the slopes from the fitting of experimental data for the blue, red and NIR emissions are $n = 2.8$, 2.7 and 1.9, respectively. These results demonstrate that the blue and red emission bands(n ~3) are predominantly populated by three-photon absorption mechanism. However, the slope value for the NIR UC emission band at 771 nm (~ 2.0) is caused predominantly by a two-photon process.

Based on the above outcomes and energy matching of levels transitions, a potencial UC-mechanism for populating the Tm^{3+}:^{1}G$_4$, ^{3}F$_3$ and ^{3}H$_4$ energy levels, under NIR excitation at 980 nm, is proposed. The approach adopted in this inquiry was to use a threefold energy transfer process between Yb^{3+} and Tm^{3+} ions to further populate the upper Tm^{3+}: ^{1}G$_4$ excited state (~ 20,000 cm^{-1}) [29, 30]. To clearly illustrate the plausible excitation mechanism and emission channels, the energy level diagram corresponding to Tm^{3+}: Yb^{3+} ions with acceptable pathways is shown in Fig. 3 [29, 30]. Initially, when the sample is excited by near-infrared radiation at λ~ 980 nm, the NIR photons are mainly absorbed by Yb^{3+} (^{2}F$_{7/2}$) ions due to its large absorption cross section at ~ 1 μm [7–10], resulting from the population of the excited Yb^{3+} (^{2}F$_{7/2}$) state. Subsequently, considering that Tm^{3+} ions cannot be directly excited by 980 nm wavelength, the Tm^{3+} ions can be promoted to the ^{3}H$_5$ manifold through energy transfer process (ET1) from Yb^{3+} ions [(ET1): Tm^{3+}(^{3}H$_6$) + Yb^{3+}(^{2}F$_{5/2}$) → Tm^{3+}(^{3}H$_5$) + Yb^{3+}(^{2}F$_{7/2}$)].
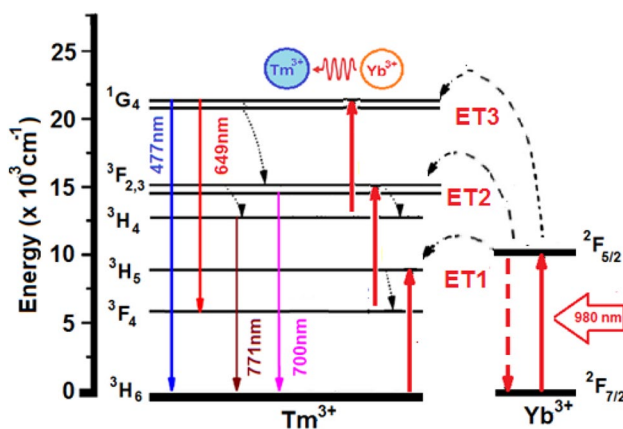

Fig. 3 Energy level diagram showing the up-conversion mechanism involving Tm^{3+}, Yb^{3+}ions. The solid lines represent radiative processes (excitation and luminescence), and dotted lines are energy transfer channels

Owing to the neighborhood to the ^{3}F$_4$ state, multi-phonon decay relaxes any population in the ^{3}H$_5$ state to the ^{3}F$_4$ state manifold. The intermediate excited state ^{3}F$_{2,3}$, from which the populations can be promoted to the lower ^{3}H$_4$ level via non-radiative mechanism, can be populated through the energy transfer process (ET2): Tm^{3+}(^{3}F$_4$) + Yb^{3+}(^{2}F$_{5/2}$) → Tm^{3+}(^{3}F$_{2,3}$) + Yb^{3+}(^{2}F$_{7/2}$). In addition to the non-radiation relaxation process to the ^{3}H$_4$ level, the population of the emitting level ^{3}F$_{2,3}$ can be depopulated through a radiation process ^{3}F$_{2,3}$ → ^{3}H$_6$ to obtain the NIR emission at 700 nm. Finally, the blue-red emitting level ^{1}G$_4$ of the Tm^{3+} ions [^{1}G$_4$ → (^{3}H$_6$, ^{3}F$_4$) transitions] could be populated considering a threefold energy transfer process between Yb^{3+} and Tm^{3+} ions [29, 30]. The currently accepted energy transfer UC luminescence mechanism is concomitant with the cubic dependence of blue-red emissions (slope of ~ 3), suggesting, effectively, that the emission level ^{1}G$_4$ has been populated by a three-photon step mechanism, including the non-radiative relaxations. Briefly, an interaction between excited Yb^{3+} ions, in the upper excited level ^{2}F$_{5/2}$, transfers their energy (ET3) to Tm^{3+} ions in the ^{3}H$_4$ manifold, promoting them to ^{1}G$_4$ excited state to yield the luminescence at the visible via ^{1}G$_4$ → ^{3}H$_6$ (blue) and ^{1}G$_4$ → ^{3}F$_4$ (red) transitions. To complete, the intense UC emission located at around 771 nm was produced due to the radiative ^{3}H$_4$ → ^{3}H$_6$ transition. Concisely summarized, the population of the NIR emitting level ^{3}F$_{2,3}$ decays by a non-radiation relaxation process to the ^{3}H$_4$ level. After that, the ^{3}H$_4$ level was populated, and at that point, the ^{3}H$_4$ → ^{3}H$_6$ transition produces the NIR emission at 771 nm.

3.3 Temperature-sensing performance UC Luminescence:

To explore the possibility of their application in luminescent thermometry, the effect of variation of the external temperature on the UC fluorescence emissions of the co-doped SrF$_2$: Tm (0.2) Yb (8.0) fluoride powder, under the excitation of 980 nm (~ 140 mW), has been monitored to investigate the sensing property of the phosphor with respect to a change in the sample temperature in the range of 298–573 K. Figure 4a exhibits the temperature-dependent emission spectra of the UC luminescence at various temperatures. The emission intensity of various peaks changes with increasing temperature, leading to the gradual quenching of the UC emission bands. The most relevant band intensity changes are observed for the ^{1}G$_4$ → ^{3}H$_6$, ^{1}G$_4$ → ^{3}F$_4$ transitions, at the visible, and for the ^{3}H$_4$ → ^{3}H$_6$ transition at the infrared. But, a fluorescence band in the near-infrared region, identified as the ^{3}F$_{2,3}$ → ^{3}H$_6$ transition, raises monotonously with the enhancement of the sample temperature. This phenomenon may be ascribed owing to the thermally induced population derived from the ^{3}H$_4$ level. As shown in Fig. 3, the energy level ^{3}F$_{2,3}$ lies above level ^{3}H$_4$ with
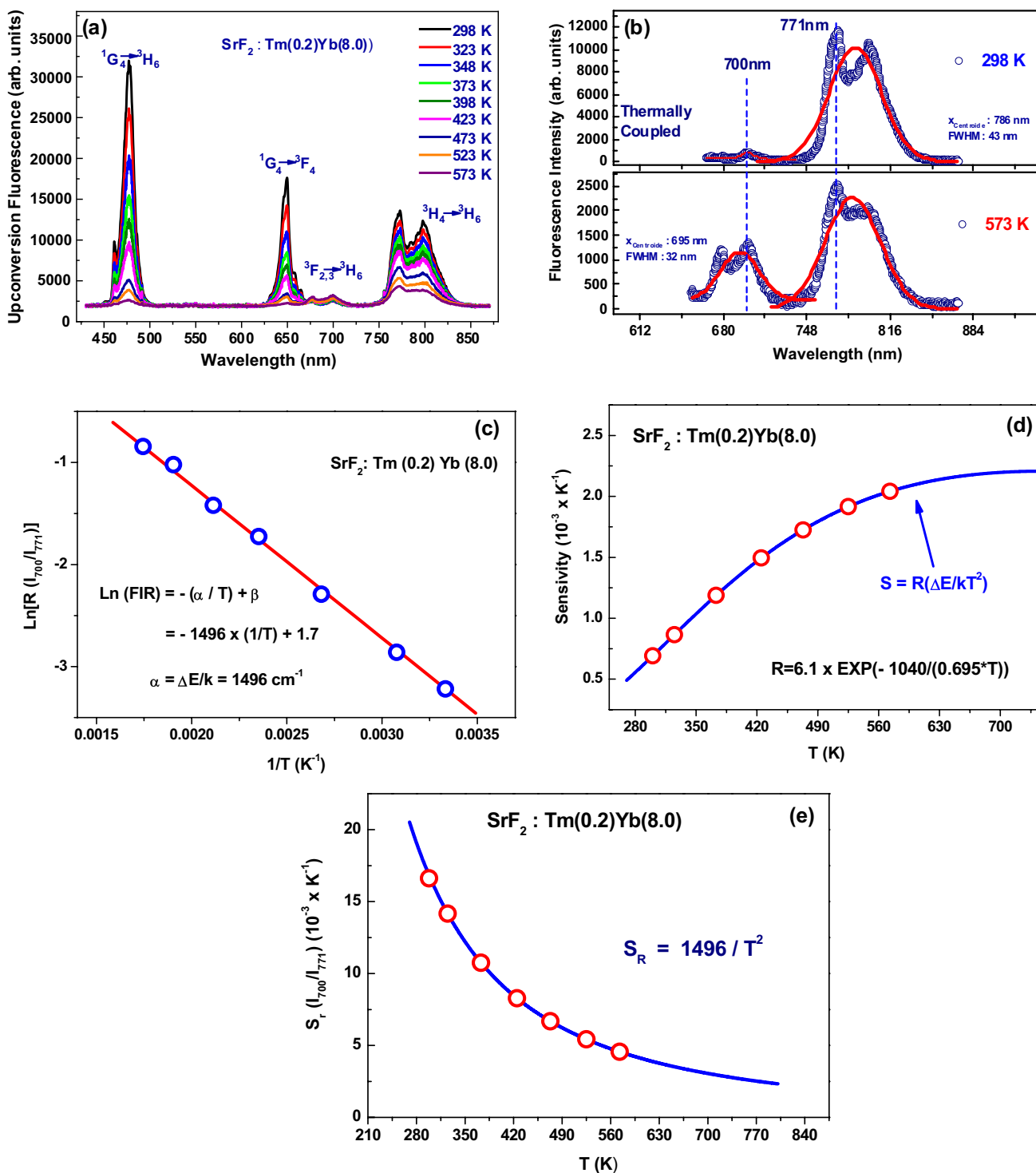
Fig. 4 a UC fluorescence spectra of SrF_2: Tm^{3+} Yb^{3+} taken at different sample temperatures ranging from 298 to 573 K upon CW 980 nm laser at 140 mW. **b** Wavelength near-infrared luminescence spectra for two thermal coupled levels at two different temperatures. The corresponding parameters (peak position, full width at half maximum (FWHM) are listed in the figure). **c** Monolog plot of the fluorescence intensity ratio for the emission bands centered at 700 and 771 nm as a function of inverse absolute temperature. **d** The absolute temperature sensitivity S_a as a function of the temperature. **E** The relative sensitivity S_r in the temperature range of 298–573 K

an energy separation about ~ 1315 cm^{-1}. When the temperature of the sample is raised, population is thermally rearranged between these states, suggesting that both levels (^{3}F$_{2,3}$ and ^{3}H$_4$) are thermally coupled. Hence, this marked difference in the quenching rates of those emission bands (^{3}F$_{2,3}$ and ^{3}H$_4$) is an indicative of a high thermal sensitivity offered by the co-doped SrF$_2$: Tm (0.2) Yb (8.0) sample.

3.3.1 Thermally coupled energy levels:

In this way, to explore the applicability of the SrF$_2$: Tm (0.2) Yb (8.0) phosphor powder for optical thermometry, the investigation of temperature-sensing behavior was focused on ^{3}F$_{2,3}$ and ^{3}H$_4$ intermediate levels owing to the thermally intensity dependence of these transitions. Figure 4(b) represents the temperature-dependent emission spectra in the near-infrared region of ^{3}F$_{2,3} \rightarrow {}^3$H$_6$ and ^{3}H$_4 \rightarrow {}^3$H$_6$ transitions. It is noteworthy that the NIR spectra display some Stark components from these transitions. These emission bands (^{3}F$_{2,3} \rightarrow {}^3$H$_6$ and ^{3}H$_4 \rightarrow {}^3$H$_6$) are fitted by Gaussian function. According to the fitting results, the energy gap between the ground state ^{3}H$_6$ and the spectral centroid of emission bands (level ^{3}F$_{2,3}$ and level ^{3}H$_4$) is obtained to be ~ 14,347 cm^{-1} and ~ 12,757 cm^{-1}, respectively, which agree well with the values tabulated in Ref. [27]. Calculated by the Gaussian fitting equation (spectral centroid), the ΔE of the thermal levels for temperature sensing is determined to be ΔE ~ 1590 cm^{-1}, too close to the value obtained directly from the spectra taken into account the most intense peak emission at 700 nm and 771 nm, respectively (ΔE:1315 cm^{-1}).

As illustrated in Fig. 4(b), a different spectral profile is observed at 573 K than that detected at 298 K. (The corresponding peak position and full width at half maximum (FWHM) are listed in the figure.) As soon as the temperature of the sample is raised, the relative intensity between these emission bands changes gradually, the intensity of ^{3}F$_{2,3} \rightarrow {}^3$H$_6$ transition increases, while the intensity of ^{3}H$_4 \rightarrow {}^3$H$_6$ transition decreases. Thus, the ^{3}F$_{2,3}$ levels may be populated from the ^{3}H$_4$ level through thermal excitation. This observation indicates a strong thermal coupling among ^{3}F$_{2,3}$ and ^{3}H$_4$ levels. It is clear that the relative intensity ratio of I$_{700}$ / I$_{771}$ rises with increasing of the sample temperature. According to the Boltzmann distribution theory, the fluorescence intensity ratio (FIR) from two thermally coupled energy levels separated in energy by ΔE can be expressed as [13–17]:

$$\text{FIR} = \frac{I_2}{I_1} = \frac{c_2(\nu_2)p_2^r \nu_2 g_2}{c_1(\nu_1)p_1^r \nu_1 g_1}\exp\left(\frac{-\Delta E}{kT}\right) = A\exp\left(\frac{-\Delta E}{kT}\right) \tag{1}$$

$$A = \frac{c_2(\nu_2)p_2^r \nu_2 g_2}{c_1(\nu_1)p_1^r \nu_1 g_1} \rightarrow \text{FIR} = A\exp\left(\frac{-\Delta E}{kT}\right),$$

I_2 and I_1 denote the integrated emission intensities for the upper and lower thermally coupled levels, respectively, A is the proportionality factor, and ΔE is the barycenter of the energy bandgap between these two coupled levels. The Boltzmann constant is represented by k, and T is the absolute temperature. The pre-exponential factor is a function of the fluorescence collection efficiency $c_i(\nu_i)$, the emission frequency ν_i, the level's degeneracy g_i and the spontaneous (radiative) emission rate p_i^r (i = 1, 2). For the purpose to acquire the relationship between FIR and T, it is required to determine the parameter $\Delta E/k$, so Eq. (1) can be converted in the form of a linear equation as

$$\text{FIR} = A\exp\left(\frac{-\Delta E}{kT}\right)\text{Ln(FIR)} = \left(\frac{-\Delta E}{kT}\right)$$
$$+ \text{Ln}A\text{Ln(FIR)} = \left(\frac{-\alpha}{T}\right) + \beta, \tag{2}$$

According to Eq. (2), the plot of the natural logarithm (Ln) of the experimental data of the FIR (Fig. 4c) as a function of the inverse of absolute temperature is expected to be a linear fitting if the temperature-controlled population obeys a Maxwell–Boltzmann distribution function. Note that the monolog plot of the experimental data yielded a linear dependence of the *FIR* with the inverse of temperature. The data are fitted with a linear curve ln [*FIR*] = —(α/T) + β, and the values for the adjustable parameters α and β are shown in Fig. 4c. The slope of the linear curve (the parameter α) is related to the sensitivity of the sensor defined as the rate in which the FIR changes with temperature and it represents, according to Eq. (1), $\Delta E/k$. The fitting parameter α = 1496 K^{-1} gives an energy bandgap ΔE of ~ 1040 cm^{-1}. The data from the UC emission spectra shown in Fig. 4a give an energy bandgap of ~ 1315 cm^{-1}.

The sensitivity of the optical temperature sensor is defined as the ratio in which the FIR changes with temperature:

$$S_a = \frac{d(\text{FIR})}{dT} = \text{FIR}x\left(\frac{\Delta E}{kT^2}\right) = A\left(\frac{\Delta E}{kT^2}\right)\exp\left(\frac{-\Delta E}{kT}\right) \tag{3}$$

and the results found for our sample are shown in Fig. 4d. The maximum sensor sensitivity found for our sample is ~ 2.1 × 10^{-3} K^{-1} at 573 K. For comparison, the optical temperature-sensing performances of Tm^{3+}/Yb^{3+}: SrF$_2$ ceramic powders in different hosts from different authors, based on the FIR technique, are listed in Table 1.

With the purpose of quantitatively presenting the practicability of temperature sensing of the Tm^{3+}/Yb^{3+}: SrF$_2$ sample, the relative temperature sensitivities, S$_r$, were calculated. The relative sensitivity S$_r$, which describes the varying rate of FIR in function of the temperature T, is expressed by:

$$S_r = \left(\frac{d(\text{FIR})}{dT}\right)\frac{1}{\text{FIR}}S_r = \left(\frac{\Delta E}{kT^2}\right) \tag{4}$$
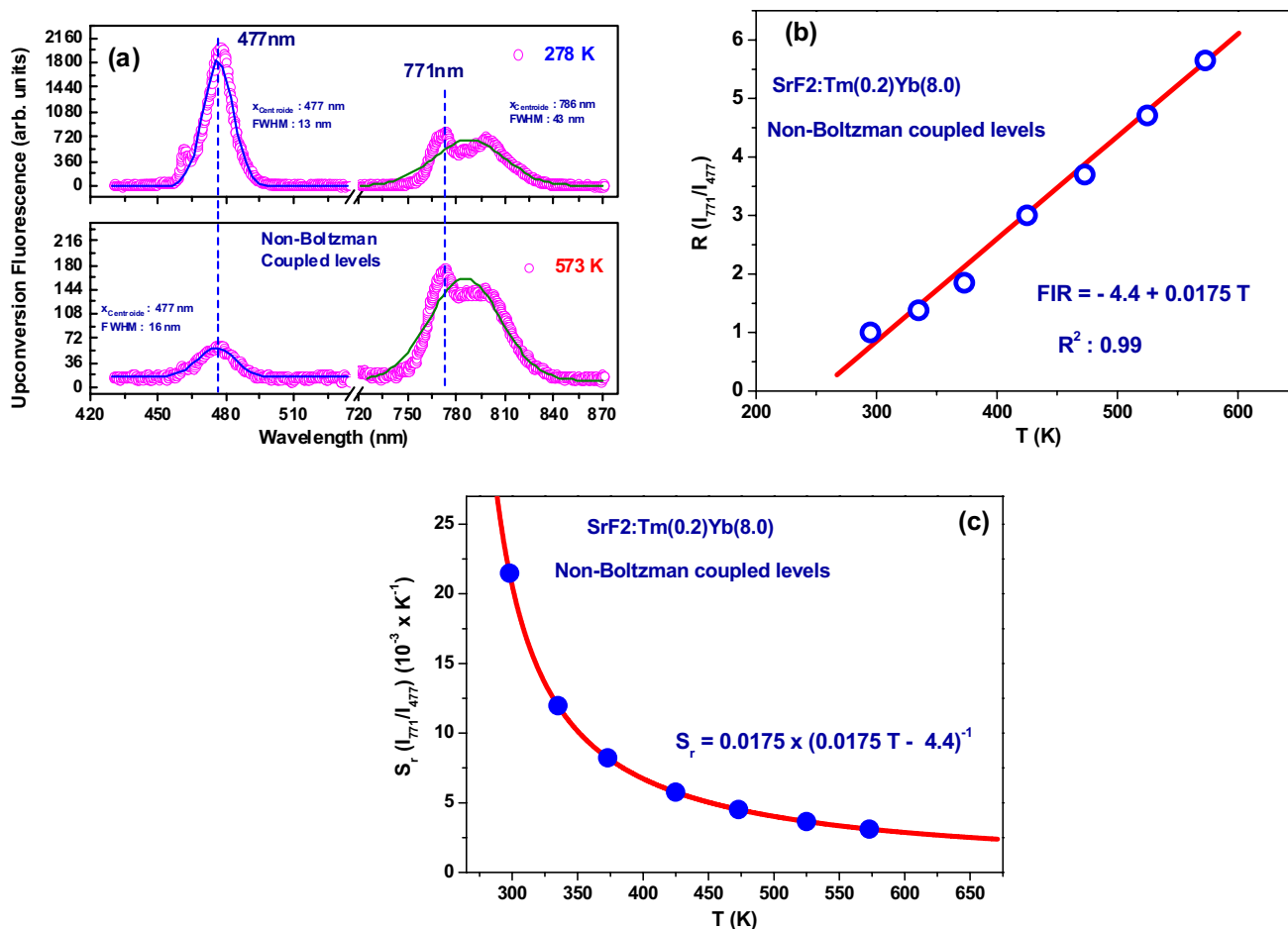
Fig. 5 **a** UC fluorescence intensity for two non-thermal coupled emission bands (NTCB) at two different temperatures. The corresponding parameters (peak position, full width at half maximum (FWHM) are listed in the figure; **b** The ratio (FIR) of two NTCB transitions $^3H_4 \rightarrow {}^3H_6$ and $^1G_4 \rightarrow {}^3H_6$ as a function of temperature. The solid line represents the linear best-fit function. **c** The relative sensitivity S_{NTr} as a function of temperature in the range of 298–573 K

By using this equation, the relative sensitivity, S_r, for the $^3F_{2,3} \rightarrow {}^3H_6$ and $^3H_4 \rightarrow {}^3H_6$ transitions was calculated and shown in Fig. 4e. The maximum S_r value based on thermal coupled levels ($^3F_{2,3}$) and ($^3H_4$) is ~ 1.7%K^{-1} at 298 K.

An estimate of the accuracy of the FIR method, for the thermally coupled energy levels $^3F_{2,3} / {}^3H_4$, is given by the error (δ):

$$\delta = \frac{|\Delta E_c - \Delta E_m|}{\Delta E_m} \tag{5}$$

where for each data set, ΔE_c is the calculated energy bandgap obtained through the slope of the linear curve fit in Fig. 5a, and ΔE_m is taken from the fluorescence spectrum shown in Fig. 2b. It was obtained an error of 20%.

3.3.2 Non-thermally coupled energy levels:

To complement the FIR thermal sensing approach from TCL method, the ratiometric variations of the fluorescence intensity from two non-thermally coupled fluorescence bands (NTCL) were exploited as a fluorescent thermometer. In this analysis, the variation in the intensity ratio of these NTCL bands will display the temperature-sensing behavior of the sample based on FIR technique. Figure 5(a) represents the temperature dependence of the UC emission spectra of Tm^{3+}: Yb^{3+}: SrF$_2$ powders excited at 980 nm and monitored in the temperature range of 298–573 K. (The corresponding peak position and full width at half maximum (FWHM) parameters are listed in the figure.) It is noted that the thermal evolution of blue (~ 477 nm) and the NIR (~ 771 nm) emissions vary with changing temperature, their fluorescence intensity integrated areas decrease as the temperature rises. What is more, the blue and NIR fluorescence bands are not equally sensitive to the variation in temperature; the fluorescence intensity of the NIR emission displays a very slight decrease in contrast to the blue emission. Thus, it is feasible to exploit the temperature information by changes

in signal intensity for both NTCB: I$_{771}$ and I$_{477}$ of the UC emission bands. Therefore, an empirical approximation has been taken in the elucidation of the influence of temperature on the ratio (FIR$_{NT}$), defined as:

$$FIR_{NT} = \frac{\text{Integrated area of NIR fluorescence}(771 \text{ nm})}{\text{Integrated area of blue fluorescence } (477 \text{nm})} \quad (6)$$

The transitions, separated by a large energy gap $\Delta E \sim 8000$ cm^{-1}, are attributed to $^3H_4 \rightarrow {}^3H_6$ (771 nm) and $^1G_4 \rightarrow {}^3H_6$ (477 nm). Figure 5b represents the temperature dependence of FIR$_{NT}$ (298–573 K). The plot of the experimental FIR$_{NT}$ versus temperature displays a nearly linear dependence on the curve parameters and could be perfectly fitted by a first-order polynomial function:

$$FIR_{NT} = \frac{I_2}{I_1} = C + DT \quad (7)$$

where C and D are parametrical constants associated with the evaluation system.

Hence, the absolute and relative sensitivities based on these NTCL can be determined as:

$$S_{NTa} = \left(\frac{d(\text{FIR})}{dT}\right) S_{NTa} = D \quad (8)$$

$$S_{NTr} = \left(\frac{d(\text{FIR})}{dT}\right)\frac{1}{\text{FIR}} S_{NTr} = \left(\frac{D}{C + DT}\right) \quad (9)$$

As depicted in Fig. 5b, the ratio of NIR (771 nm) to blue (477 nm) increases with temperature and is observed a linear response. Thus, the experimental results could be linearly fitted by the formula FIR = 4.4 + 0.0175 T. The correlation coefficient of the linear curve fitting was calculated to be $R^2 = 0.99$. The corresponding values of sensor relative sensitivity S_{NTR} as a function of temperature were calculated and plotted in Fig. 5(c). The maximum relative sensitivity is $\sim 2.2\%$ K^{-1} at 298 K.

The above results reveal that Tm^{3+}: Yb^{3+}: SrF$_2$ phosphor offers a good fluorescence response when adopting the NTCL approach following a linear FIR$_{NT}$ fluorescence intensity temperature dependence.

4 Conclusions

In summary, we successfully prepared Tm^{3+}: Yb^{3+}: SrF$_2$ ceramic powders with variable dopant concentrations through a simple combustion synthesis route at 500 ^{0}C for 20 min. Upon the excitation of 980 nm laser diode, the characteristics of UC luminescence and optical temperature sensing are studied. Through the sensitization of Yb^{3+} to Tm^{3+}, up-conversion luminescence exhibit four emission bands in

the range of 400 to 900 nm. The strongest emission peak of Tm^{3+} in SrF$_2$ host was found at 477 nm and is attributed to the $^1G_4 \rightarrow {}^3H_6$ transition. The intensity of each emission bands shows a significant temperature-dependent behavior that can be used for temperature-sensing purposes. Thermal sensing performances based on fluorescence intensity ratio based on both thermally and non-thermally coupled energy levels were proposed for the explored system in the 298–573 K range. Through examining the temperature-sensing performance for TCL [($^3F_{2,3} \rightarrow {}^3H_6$) and ($^3H_4 \rightarrow {}^3H_6$)], the material showed a high-temperature sensitivity, around 2.1×10^{-3} K^{-1}, and a relative sensitivity of 1.7% at 298 K. Furthermore, by using the FIR changes as a function of temperature based on NTCB, the relative sensitivity was determined to be 2.2% K^{-1} at 298 K based on $^3H_4$ (NIR emission) and $^1G_4$ (blue emission) radiate bands. The use of a NTCL methodology allowed the optimization of the FIR performance to be carried out with a TCB technique.

These results promote luminescent Tm^{3+}: Yb^{3+}: SrF$_2$ powders for thermometry applications to be used as non-contact fluorescence probe following two different approaches based on the FIR ratio of thermally and non-thermally coupled energy levels.

Declarations

Conflict of interest On behalf of all authors, the corresponding author states that there is no conflict of interest.

References

1. N. Rakov, G.S. Maciel, RSC Adv. (2015). https://doi.org/10.1039/C4RA15804K
2. M. Shang, C. Li, J. Lin. Chem. Soc. Rev. (2014). https://doi.org/10.1039/C3CS60314H
3. G. Chen, C. Yang, P.N. Prasad, Acc. Chem. Res. (2013). https://doi.org/10.1021/ar300270y
4. F. Auzel, Chem. Rev. (2004). https://doi.org/10.1021/cr020357g
5. B. Jacquier, G. Liu.(Eds.) Spectroscopic Properties of Rare Earths in Opt. Mater; edn. (Springer, Berlin. 2010).
6. W. Yang, X. Li, D. Chi, H. Zhang, X. Liu. Nanotechnol. (2014) http://iopscience.iop.org/0957-4484/25/48/482001
7. L. Meisong, L. Shunguang, S. Hongtao, F. Yongzheng, H. Lili, Z. Junjie, Mater. Lett. (2006). https://doi.org/10.1016/j.matlet.2005.12.022
8. H. Guo, N. Dong, M. Yin, W. Zhang, L. Lou, S. Xia, J. Phys. Chem. B (2004). https://doi.org/10.1021/jp048072q

9. I. Etchart, I. Hernandez, A. Huignard, M. Berard, M. Laroche, W.P. Gillin, R.J. Curry, A.K. Cheetham, J. Appl. Phys. (2011). https://doi.org/10.1063/1.3549634

10. A. Patra, S. Saha, M.A.R.C. Alencar, N. Rakov, G.S. Maciel, Chem. Phys. Lett. (2005). https://doi.org/10.1016/j.cplett.2005.03.135

11. N. Rakov, Y. Xing, G.S. Maciel, ACS Appl. Nano Mater. (2020). https://doi.org/10.1021/acsanm.0c02397

12. H. Zhou, M. Sharma, O. Berezin, D. Zuckerman, M.Y. Berezin, Chem. Phys. Chem (2016). https://doi.org/10.1002/cphc.201500753

13. S.A. Wade, S.F. Collins, G.W. Baxter, J. Appl. Phys. (2003). https://doi.org/10.1063/1.1606526

14. J. Zhang, YQ. Zhang, XM, Jiang. (2018) J. Alloys Compd. doi: https://doi.org/10.1016/j.jallcom.2018.03.127

15. W. Xu, X. Gao, L. Zheng, Z. Zhang, W. Cao, Sens. Actuators B. (2012). https://doi.org/10.1016/j.snb.2012.07.009

16. P. Cortelletti, C. Facciotti, I.X. Cantarelli, P. Canton, M. Quintanilla, F. Vetrone, A. Speghini, M. Pedroni, Opt. Mater (2017). https://doi.org/10.1016/j.optmat.2016.11.019

17. M. Quintanilla, Y. Zhang, L.M. Liz-Marzan, Chem. Mater. (2018). https://doi.org/10.1021/acs.chemmater.8b00806

18. H. Lu, H. Hao, Y. Gao, D. Li, G. Shi, Y. Song, Y. Wang, X. Zhang, Microchim. Acta. (2017). https://doi.org/10.1007/s00604-016-2070-6

19. G. Chen, R. Lei, H. Wang, F. Huang, S. Zhao, S. Xu, Opt. Mater (2018). https://doi.org/10.1016/j.optmat.2018.01.039

20. A. Kumari, A. Pandey, R. Dey, V.K. Rai, RSC Adv. (2014). https://doi.org/10.1039/C4RA01400F

21. M. Jiao, L. Jing, C. Liu, J. Huang, X. Wei, M. Gao, Chem. Commun. (2016). https://doi.org/10.1039/C6CC01686C

22. D. Tian, D. Gao, B. Chong, X. Liu, Dalton Trans. (2015). https://doi.org/10.1039/C4DT03735A

23. M.B. Seelbinder, J.C. Wright, Phys. Rev. B. (1979). https://doi.org/10.1103/PhysRevB.20.4308

24. A.A. Lyapin, S.V. Gushchin, S.V. Kuznetsov, P.A. Ryabochkina, A.S. Ermakov, VYu. Proydakova, V.V. Voronov, P.P. Fedorov, S.A. Artemov, A.D. Yapryntsev, V.K. Ivanov, Opt. Mater. Express. (2018). https://doi.org/10.1364/OME.8.001863

25. N. Rakov, G.S. Maciel, Curr. Appl. Phys. (2017). https://doi.org/10.1016/j.cap.2017.06.001

26. Y. Zhang, S. Xu, X. Li, J. Sun, J. Zhang, H. Zheng, H. Zhong, R. Hua, H. Xia, B. Chen, J. Alloys Compd. (2017). https://doi.org/10.1016/j.jallcom.2017.03.125

27. L. Xing, Y. Xu, R. Wang, W. Xu, Z. Zhang, Optic. Lett. (2014). https://doi.org/10.1364/OL.39.000454

28. Carnall, W. T., Crosswhite, Hannah, and Crosswhite, H. M. Energy level structure and transition probabilities in the spectra of the trivalent lanthanides in LaF3, (United States: N. p., 1978), doi:https://doi.org/10.2172/6417825

29. M. Misiak, K. Prorok, B. Cichy, A. Bednarkiewicz, W. Strek, Optical Mater. (2013). https://doi.org/10.1016/j.optmat.2013.01.002

30. F.W. Ostermayer, J.P. van der Ziel, H.M. Marcos, L.G. Van Uitert, J.E. Geusic, Phys. Rev. B **3**, 2698–2705 (1971)